High-temperature Magnetodielectric Bi(Fe$_{0.5}$Mn$_{0.5}$)O$_3$ Thin Films with Checkerboard-Ordered Oxygen Vacancies and Low Magnetic Damping

E. Coy,[1,*] I. Fina,[2,3] K. Załęski,[1] A. Krysztofik,[4] L. Yate,[5] L. Rodriguez,[3] P. Graczyk,[4] H. Głowiński,[4] C. Ferrater,[3] J. Dubowik,[4] and M. Varela[3]

[1]*NanoBioMedical Centre, Adam Mickiewicz University, ul. Umultowska 85, 61-614 Poznań, Poland*
[2]*Institut de Ciència de Materials de Barcelona (ICMAB-CSIC), Campus UAB, Bellaterra, 08193 Barcelona, Spain*
[3]*Departament de Física Aplicada, Universitat de Barcelona, Carrer de Martí i Franquès, 1, 08028 Barcelona, Spain*
[4]*Institute of Molecular Physics, Polish Academy of Sciences, ul. Smoluchowskiego 17, 60-179 Poznań, Poland*
[5]*CIC biomaGUNE, Paseo Miramón 182, 20014 Donostia-San Sebastian, Spain*

The possibility of affecting the magnetic properties of a material by dielectric means, and vice versa, remains an attractive perspective for modern electronics and spintronics. Here, we report on epitaxial Bi(Fe$_{0.5}$Mn$_{0.5}$)O$_3$ thin films with exceptionally low Gilbert damping and magnetoelectric coupling above room temperature (< 400 K). The ferromagnetic order, not observed in bulk, has been detected with a total magnetization of 0.44 μ_B/formula units with low Gilbert damping parameter (0.0034), both at room temperature. Additionally, a previously overlooked check-board ordering of oxygen vacancies is observed, providing insights on the magnetic and dielectric origin of the multifunctional properties of the films. Finally, intrinsic magnetodielectric behavior is observed as revealed by the variation of dielectric permittivity well above room temperature. These findings show the possibility of electric-field-controlled magnetic properties, in low Gilbert-damping-based spintronic devices, using single-phase multiferroic materials.

I. INTRODUCTION

Multiferroic materials have been the focus of the scientific community's attention due to their potential application for energy efficient data storage [1]. The study of multiferroic double perovskites ($A_2BB^*O_6$) is of high interest, because complex interactions taking place between the B-B^* ions might promote both ferromagnetic (FM) and antiferromagnetic (AFM) orderings due to the superexchange interactions between filled and half-filled orbitals [2,3]. Traditionally, while the magnetic properties are controlled by the B-site ions, the A ions would deal with the ferroelectric (FE) ordering, by placing atoms with lone pair electrons, such as Bi or Pb [4,5]. The presence of these ions is responsible for the crystal structure symmetry breaking [6,7] and the generation of spontaneous polarization. Among the double perovskites, the ferromagnetic La$_2$NiMnO$_6$ [8–15], and multiferroic Y$_2$NiMnO$_6$ [16–22], Bi$_2$NiMnO$_6$ [4,23–27] are among the most promising and broadly studied. However, ferroelectric and ferromagnetic coexistence has encouraged the disparate Bi-based double perovskites, such as Bi$_2$CoMnO$_6$ [28] and Bi$_2$FeMnO$_6$, to be revisited [29–37].

Bi$_2$FeMnO$_6$ (BFMO) lies between two of the most well-studied multiferroic materials in the field, BiFeO$_3$ (BFO) [38,39] and BiMnO$_3$ (BMO) [40,41], the characteristics of which are well described in the literature and still gain considerable attention among researchers. The interest in BiFeO$_3$ originates due to the stable ferroelectric and antiferromagnetic ordering at room temperature [42] (Néel temperature $T_N \approx 643$ K). However, BiFeO$_3$ has a low magnetic moment in bulk and thin-film form (approximately equal to 0.02 μ_B/Fe) [43–46], hindering desired applications. On the other hand, BiMnO$_3$ is the only material where the coexistence of ferromagnetic and ferroelectric order is well established [41,47]. Although FE order is present above room temperature (Curie temperature $T_C \approx 450$ K), the FM ordering appears at a rather low temperature $T_C \approx 105$ K [48], thus efforts on the study of highly doped BiMnO$_3$ to increase FM Curie temperature have been carried out in the literature [6,47]. These studies include the B-site partial substitution, such as in the case on Bi$_2$CoMnO$_6$ and Bi$_2$NiMnO$_6$ [4,25,27,28,49,50]. Nevertheless, recent experimental results on Bi(Mn$_x$Fe$_{1−x}$)O$_3$,

---

*[*]coyeme@amu.edu.pl

with $x = 0.5$ have driven new attention to this compound [30,51].

Considerable attention has been focused on understanding the magnetic properties of $Bi(Mn_xFe_{1-x})O_3$ with $x = 0.0$–0.2 in bulk [31,42] and $x = 0.5$ in rather thick films [31] by neutron diffraction. A G-type antiferromagnetic spin structure with a Néel temperature of $T_N = 120$ K has been reported [35]. In bulk however, these compounds are very difficult to stabilize unless high pressures are employed [25]. The common approach is to dope the structure with considerable quantities of lanthanum, however, such an approach complicates the distinction between intrinsic effect and dopant effects in both magnetic and crystalline properties [49,52]. Polycrystalline solid solutions show a distinctive magnetic response, with a very low magnetic moment $0.02\mu_B$/formula units (f.u.), $x = 0.2\%$. Thin-film studies, however, have shown a small increment of magnetization with $0 \leq x \leq 0.5$ of Mn substitution, while highly strained films, with partial substitution of $x = 0.5$ exhibited strong room-temperature magnetism. The work reported by Choi *et al.* [34], showed an increment on the magnetization to rather competitive levels, approximately 0.58 μ_B/B-site ion at room temperature. The important enhancement of the magnetic properties was attributed to the high level of strain induced by the epitaxial growth. However, no ferroelectric response was reported, or the ferroelectric cycle.

Additionally, electrical measurements performed on the mixed B-site $Bi(Mn_{0.5}Fe_{0.5})O_3$ thin films, have already been performed in the literature [37], showing a typical relaxor behavior in a film of 180 nm thickness. The lack of "strong" magnetism in those results seems to suggest that such a behavior is closely related to the bulk behavior rather than to the highly strained film one [53], due to the role of epitaxial strain in the stabilization of the trigonal phase and its strong magnetism. Therefore, such measurements are not compatible with the highly strained thin-film scenario, and thus the dielectric behavior of highly strained BFMO thin films is still unknown. Later reports by Choi *et al.* [54] have addressed the magnetic response of thin films with different epitaxial strain. Additionally, from the dielectric point of view, the switchable $(180°)$ response of the films is unequivocally shown by piezoelectric force microscopy. Nevertheless, conclusive magnetodielectric response or any correlation between ferroic orders have yet to be investigated.

Furthermore, although the magnetic nature of the highly strained material is quite well established to date, the magnetic damping of the BFMO is not. Magnetic relaxation processes play an important role in the magnetization switching speed and switching power of spin-transfer-torque- (STT-)based devices, especially for materials where the total magnetization is relatively low, since it directly translates into low switching currents [55,56]. Possibly more exciting are the important and intrinsic applications that a ferromagnetic material with strong magnetodielectric coupling could provide in the spin-wave propagation field. As shown in recent studies conducted on $BiFeO_3$-based spin-wave devices [57,58], there is an interesting applicability of multiferroic materials as generators, guides, and controllers for magnonic devices.

Having shown the current scenario of BFMO thin films, it is clear that experimental confirmation of magnetodielectric response, in a multiferroic (ferroelectric and ferromagnetic) materials, with low magnetic damping, is an appealing perspective for both the multiferroic and spin-wave community. Therefore, here we focus on the magnetic and magnetodielectric properties of highly strained thin films deposited by pulsed-laser deposition (PLD). First, we show the structural quality of the films, in particular, the existence of coordinated oxygen vacancies, contributing to the relaxor behavior of the perovskite. Then, we explore the magnetic response of the samples confirming the presence of low-magnetization damping, which along with the low magnetization make this material appealing for STT devices. Finally, we will show that the dielectric response of the films can be externally affected by a magnetic field well above room temperature, clearly showing evidence of strong magnetodielectric coupling in this material.

II. EXPERIMENTAL DETAILS

A. Film deposition

Films (approximately equal to 43 nm) are deposited by a KrF excimer laser (248 nm) by Lambda Physik LPC205i, focused on a stoichiometric ceramic target with a bismuth excess of 10%. Samples are grown on two substrates $SrTiO_3(001)$ (STO), used for magnetic measurements, and $Nb(0.5\%):SrTiO_3(001)$, used for dielectric measurements. Substrate temperature is set to $650\,°C$ according to optimization studies performed on this material and similar compounds in order to avoid losses of bismuth during deposition [25,59]. Depositing conditions are set as follows: oxygen pressure at 0.6 mbar, ablation rate at 5 Hz, and laser fluency at approximately 1.7 J cm^{-2}.

B. Structural characterization

X-ray diffractograms (XRD) and reciprocal space maps (RPMs) are obtained using a PANalytical X'Pert3 (MRD) system, working with a Cu source (K_α 0.15406 nm). Microstructure is investigated by high-resolution (HR) TEM using a JEOL ARM200F working in the scanning mode. An accelerating voltage of 200 kV is used to perform structural characterization. Cross sections are prepared by FIB milling using a JEOL JIB-4000. A gold film is sputtered on top of the selected area to protect it from ion damage during the FIB milling. A Ga^+ beam with different acceleration voltages (5–30 kV) is used to prepare the cross sections. Stoichiometry and valence of the films

(Bi, Fe, and Mn ions) are studied by x-ray photoelectron spectroscopy (XPS) using a SAGE HR100 (SPECS) system with a nonmonochromatic source (Al K_α 1486.6 eV). Calibration of the spectra is performed by placing the C-C carbon peak at 284.8 eV. Crystallographic structures are build using the CaRine 4.0 software.

C. Functional characterization

Magnetic measurements are performed by a SQUID magnetometer using a Quantum Design MPMS XL-7 system. Magnetization dynamics is investigated using vector network analyzer ferromagnetic resonance (VNA FMR) in the range of 3–30 GHz under a maximum external field of 10 kOe. The applied frequencies are kept constant while the magnetic field is swept. To enhance the FMR signal, the Au-coating is applied to the back side of the substrates [60]. The samples are placed with the film facing towards the coplanar waveguide (CPW), where the impedance changes at resonance causing a change in the S21 transmission signal detected by VNA. The obtained resonance lines are fitted with a Lorentz function giving the resonance field and the resonance linewidth, and allowing for the determination of magnetization and Gilbert damping constants.

Impedance spectroscopy (IS) measurements are performed by means of an impedance analyzer (HP4129 LF, Agilent Co.) with an excitation voltage of 50 mV at frequencies ranging from 10 Hz to 10 MHz. Samples are placed on a Lakeshore 4 tip probe station with nitrogen gas flow working from 90 to 400 K. Samples are measured in the so-called top-top configuration [61], using sputtered Pt electrodes (60 μm in diameter). Magnetic impedance measurements are performed by placing a neodymium solid-state magnet providing a total effective field approximately equal to 4 kOe, underneath the sample holder after full range sweeps. The magnitude of the magnetic field at the sample position is tested by Gaussmeter measurement. Impedance data is analyzed in order to extract the intrinsic dielectric permittivity of the film, as described below, following analyzes described elsewhere [16,49,52].

III. EXPERIMENTAL RESULTS

A. Structure and composition

X-ray studies show the high crystallinity of the film. Figure 1(a) shows the typical 2Θ-ω scans of the samples, where only the BFMO(00l) peaks are visible with no secondary phases or orientations. BFMO films are flat with a thickness of approximately 43.5 ± 1.2 nm, as extracted from XRR scans [Fig. 1(b)] using the PANalytical X'pert reflectivity software. The extracted roughness (Rq) is comparable to the one found by AFM, $Rq \approx 1.4 \pm 0.3$ nm. The 2Θ-ω scans closely resemble the ones observed in single perovskites of $BiMnO_3$/STO(001) [35,47,62] and $BiFeO_3$/STO(001) [58,63–66].

According to the interplanar distance of d[00l] and both the Bragg equation and the Nelson-Riley correction, the out-of-plane parameter of the BFMO unit cell is calculated as being approximately equal to 3.99 Å. Asymmetrical measurements (ϕ scans) performed along the STO(110) direction, are shown in Fig. 1(c). Results clearly show the cube-on-cube orientation of the BFMO film with respect to the STO substrate. Moreover, the reciprocal space maps, Fig. 1(d), show that in fact the BFMO layer is fully epitaxial and strained. This observation is congruent with other reports in the literature regarding BFMO [34,39,54]. Additionally, the in-plane parameter of the BFMO is also extracted by using the $a = 2/\lambda \times h/q_x$ formula, where λ is the K_α value of Cu, q_x represents the horizontal value in reciprocal coordinates, and q_x is defined by $q_x = \sin\Theta \sin(\Theta - \omega)$. The lattice parameters extracted from the x-ray experiments are similar to those reported by Choi *et al.* [34] with $a = b = 3.93 \pm 0.02$ Å and $c = 3.99 \pm 0.02$ Å, corresponding to a compressive stress of -0.64% of in-plane stress and a total deformation of -2.81% from the bulk-simulated lattice, as shown in Table I. It is important to remark that although the relaxation thickness, in which the highly strained lattice returns to the relaxed state is unknown, studies in other perovskites congruently indicate the critical thicknesses above 70 nm [68]. Thus, it is important to keep the films in their highly strained thickness approximately equal to 40 nm, in order to conclusively show the interplay between ferromagnetic ordering (observed in the highly strained samples) and ferroelectric response.

Microstructure of the films is investigated by HR TEM, general results are shown in Fig. 2(a). Insets show the low-magnification view of the film allowing the total thickness of the film 43.5 ± 1.2 nm to be extracted in agreement with XRR. Also, the inverse fast Fourier transformation (IFFT), performed using the in-plane (100) and ($\bar{1}$00) diffraction peaks, for both the substrate and the films, show the perfect matching of the lattices [inset in Fig. 2(a)]. Additionally, the high-resolution images show the high-ordered STO(001) and BFMO(001) structures pointing to the B sites of the BFMO perovskite. Selected 100 nm width area of electron diffraction (SAED) is collected, which includes reflections from the substrate and the film, and is presented in Fig. 2(b). The high-intensity peaks of the STO structure (red dashed line) overlap with those of the BFMO structure (blue dashed lines). Nevertheless, due to the difference in the out-of-plane parameter between the film and substrate, the peaks at higher-order reflections (002) and (00$\bar{2}$) are well separated, as shown by the top or the bottom of the image [circled areas in Fig. 2(b)]. Additionally, the SAED pattern shows the presence of small, well-distributed peaks (marked in yellow). The presence of those peaks is a signature of superior organization of the perovskites, which clearly follows the film reflection, as seen in the yellow squared segment of Fig. 2(b), where
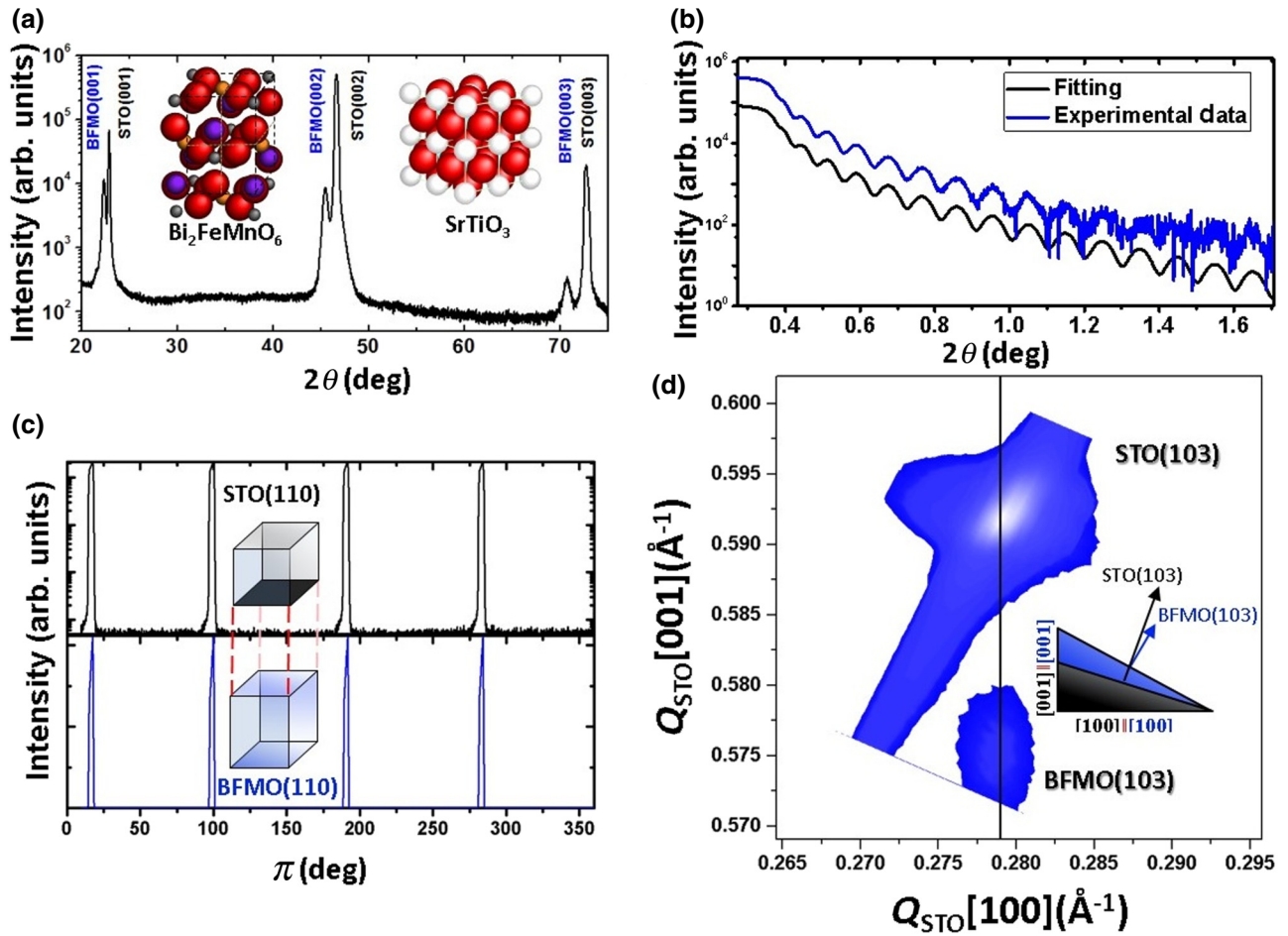
FIG. 1. Structural data of 40 nm BFMO/STO(001) film. (a) The 2Θ-ω scan shows the (001) texture of the film. Insets show a standard STO unit cell and the bulk Bi_2FeMnO_6 cells (see Table I). (b) X-ray reflectometry experiments with an extracted thickness of approximately 43.5 nm and $Rq \approx 1.2$ nm (fitting has been shifted down for clarity). (c) ϕ scans performed around the STO(110) and BFMO(110) peak position showing cube-on-cube growth as sketched. (d) Reciprocal space map around the substrate (103) reflection. The black line serves as a guide for the eye showing coincidence of BFMO and STO in-plane peak position.

the center of the small peaks is centered on the BFMO peaks. In order to understand the observed reflections, a unit cell of four times the nominal size of the BFMO unit cell is built. The atomic positions of the elements are calculated accordingly to a 4×4 BFMO unit cell. It is important to remark that two cases are considered, *B*-site ordered and *B*-site mixed, and both of the scenarios proved not to be compatible with the observed diffraction peaks. Nevertheless, the periodicity and locations of the supercell patterns can be extracted, as shown in Figs. 2(c) and 2(d), the periodicity follows a cell that is approximately equal to 1.28 nm. The nature of this cell is then evidenced by the location and geometry of the simulated lattice, corresponding to ordered oxygen vacancies on the BFMO lattice, which is further confirmed by the SAED pattern and the angular bright-field (ABF) images. Those vacancies have been observed in other perovskite systems, and the ordering is considered to affect the magnetic properties of the perovskites [69,70]. Equally important, the

clear ordering of the O-site vacancies, Fig. 2(b), might contribute to the already relaxor and nanopolar ferroelectric ordering in BFMO films [29,31,33,53,71].

The film stoichiometry is investigated by XPS. The survey spectrum of the film surface [Fig. S1(a) in Ref. [72]] shows the nominal composition of the Bi_2FeMnO_6 perovskite. High-resolution Bi $4f$ spectra shows the single Bi^{3+} [73] valence of the *A*-site cation [Fig. S1(b) in Ref. [72]]. Regarding the *B* site, although the iron Fe $2p$ region is quite complex to analyze [74,75], the peak position and its shape is congruent with Fe^{3+} and traces of Fe^{2+} [Fig. S1(c) in Ref. [72]], while the Mn $2p$ shows a slight mixture of Mn^{3+} and Mn^{4+} [75], which confirm the observations of Ahmed *et al.* [76] [Fig. S1d in Ref. [72]]. Attempts of cleaning the surface and performing depth-profiling studies by Ar^+ plasma etching, results in the expected valence shifts of the iron ions moving towards metallic Fe^0, [74,75], while Mn and Bi show [77] consistent values of Mn^{4+} and Bi^{3+}, respectively [Fig. S1(d) in

TABLE I.   Lattice constants of BFMO thin films and bulk material.

	a (Å)	b (Å)	c (Å)	$\varepsilon_{[110]}$ (%)[a]	$f_{[010]}$ (%)[b]
Bi_2FeMnO_6 (films)	3.93 ± 0.02	3.93 ± 0.02	3.99 ± 0.02	-2.81	-0.64
Bi_2FeMnO_6 (bulk) [67]	5.7184	5.7184	8.087	$\cdots$	-3.43
$(Fe^{3+}Mn^{3+})$ [30]	5.5579	5.5579	8.060	$\cdots$	-0.64
	x	y	z		
$Bi^{(3+)}$	1/2	1/2	1/4		
$Fe^{(2+)/(3+)}$	0	1/2	0		
$Mn^{(4+)/(3+)}$	1/2	0	0		
$O^{(2-)}$	0.2647	0.2356	0		
$O^{(2-)}$	0.2647	13/17	0		
$O^{(2-)}$	1/2	0	0.2353		

[a]The stress as $100\% \times (n_{film} - n_{bulk})/n_{bulk}$, where n_{bulk} is the in-plane lattice of $Bi_2FeMnO_6/\sqrt{2}$.
[b]The lattice mismatch as $100\% \times (a_{substrate} - a_{film})/a_{film}$, where $a_{substrate}$ and a_{film} are the substrate and films lattice constants. Bulk material is assigned to the $P4/mbc$ space group. Notice that calculations performed with Fe^{3+} and Mn^{3+} give differences of less than 0.5% to the one presented.

Ref. [72]]. Although the Fe profiling cannot be fully reliable due to the large reducing effects, the Mn peaks are less susceptible to the Ar^+ damage and allow a scenario of single Bi^{3+} and Mn^{4+} valence to be suggested, while leaving the Fe valence uncertain. Nevertheless, profiling is needed in order to avoid the mixed states, or recombination of valences, that tend to appear at the outer surface of these materials [78]. Nonetheless, these results show an interesting scenario, in which both nanopolar ordering and valence compensation could coexist in this perovskite. To sum up this section, our results follow the high mixture of valences in this perovskite and complex polar orderings [39,79,80].

B. Magnetic properties

The results of magnetic studies are shown in Fig. 3. First, the field-cooled [$M(T)$] and hysteresis [$M(H)$] loops are performed under in-plane applied field. In the $M(T)$ measurements [Fig. S2 in Ref. [72]], temperature is swept from room temperature down to 5 K and allowed for the determination of transition temperature T_C as explained below. The $M(H)$ plots confirmed the ferromagnetic ordering of the film in the whole range of available temperatures, as shown by the hysteresis loops at room temperature, Fig. 3(a) and at 10 K [Fig. S2 in Ref. [72]]. The total magnetization of the film is calculated according to the B-site (Fe-Mn) ordering as 0.48 μ_B/f.u. (Fe-Mn), which is congruent with the data reported in the literature for these films [34,39].

To determine suitability of BFMO for spintronic and magnonic applications, the magnetization dynamics is investigated. Using Kittel's dispersion relation without an anisotropy term,

$$f = \frac{\gamma}{2\pi}\sqrt{H_r(H_r + 4\pi M_s)},\qquad(1)$$

where H_r is the resonance magnetic field, $\gamma = 1.76 \times 10^7$ G^{-1} s^{-1} is the gyromagnetic ratio, the saturation magnetization M_s equal to 68.8 emu/cm³ (0.44 μ_B/f.u.) is derived in agreement with the value from SQUID magnetometry and previous literature studies [34,39] [see the inset of Fig. 3(b)]. From resonance linewidth ΔH vs frequency f dependence, the Gilbert damping parameter α is determined according to the equation $\Delta H = (4\pi\alpha/\gamma)f + \Delta H_0$, where ΔH_0 is related to extrinsic contributions such as sample inhomogeneities and two-magnon scattering [Fig. 3(b)]. The fitting is performed for the frequencies above 9 GHz corresponding to the field of 2.8 kOe. At lower frequencies, depicted by the shaded area, the data significantly deviates from linear dependence. For the fields in the range 0–2 kOe the magnetization is not saturated magnetically [see Fig. 3(a)], which consequently leads to substantial line broadening [81], as shown in Fig. S3 in Ref. [72]. The α constant is equal to 0.0034, which settles the BFMO among the so-called low-damping materials [Table S-I in Ref. [72]]. The ΔH_0 is equal to 5.34 Oe pointing to the flat film surfaces (as proved with x-ray reflectometry), homogeneity of the sample, and negligible two-magnon scattering contribution for the in-plane applied magnetic field.

C. Magnetodielectric characterization

Dielectric studies are carried out using a temperature-dependent impedance spectroscopy method in the top-top configuration. The typical behavior of a ferroelectric relaxor is evidenced by a shift in both the imaginary part of the dielectric permittivity (ε') and the real part (ε'') vs temperature, with variations of frequency [Fig. 3(c)]. Although the origin of this behavior is not clearly understood, it is a common feature characterizing this kind of ferroelectrics. A similar behavior has already been reported
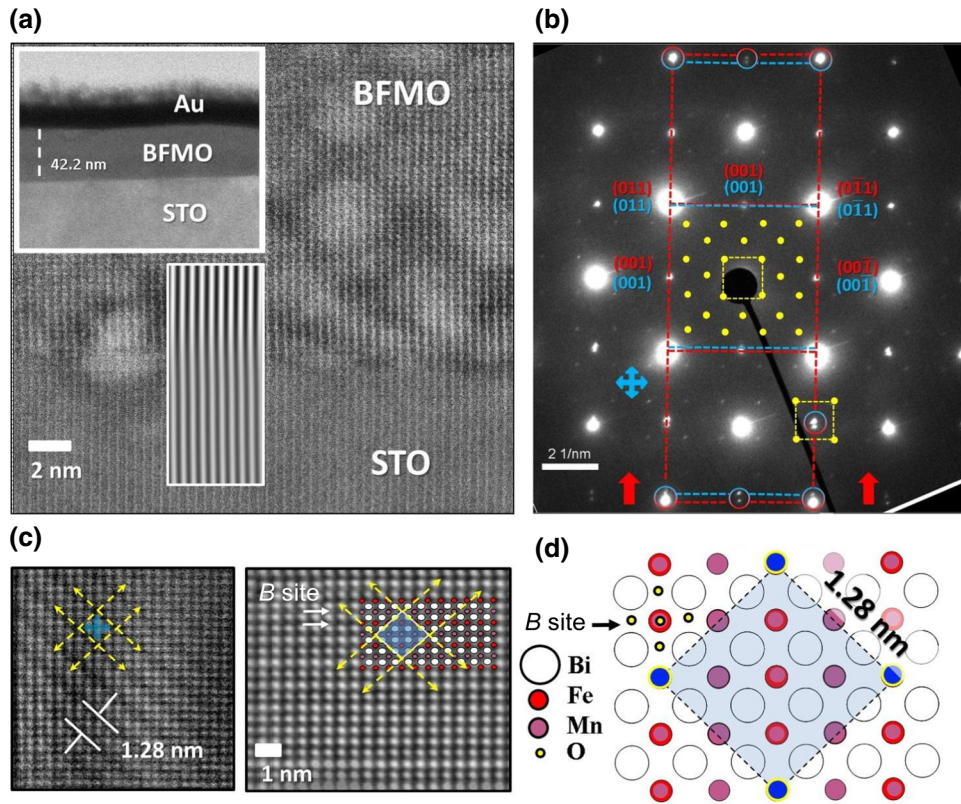
FIG. 2.   Transmission electron micrographs. (a) Low-magnification image of the films, showing the total thickness. Inset shows the interface congruence based in IFFT images. (b) SAED image collected from the film and substrate area. Bottom red arrows show the growth direction. Large dashed squares (red) represent the STO diffraction peaks. The slightly reduced dashed square (blue) represents the BFMO lattice constants. The small dashed square (yellow) shows the alignment of the supercell peaks with the BFMO peaks. Small dots in the center of the image (yellow) show the position of the larger order peaks. (c) High-resolution image showing the origin of the small ordering observed in the SAED pattern and the corresponding organization in the BFMO lattice (left) and filtered image taking the high-order peaks with an inset of the crystal correspondence. (d) Atomic configuration of the ordered oxygen vacancies are shown in blue.

in the literature for BFMO [82] and for other materials with nanopolar regions [83–86].

Using the impedance spectra (Z'/Z'') and by representing the temperature-dependent curves as Nyquist plots [Fig. 3(d)], the presence of two dielectric contributions can be observed. This representation is vital in order to avoid the confusion of intrinsic and extrinsic effects [87]. These two contributions, one at high frequencies and the other at low, have been explored before in single-perovskite thin films (BMO and BFO [88]) as well as for double perovskites [49,89]. It is clear by now that each contribution is related to a different mechanism, with the high-frequency contribution, containing the intrinsic properties of the perovskite, while the low frequencies represent the extrinsic effects in the compound and experimental setup. These two mechanisms respond differently in the impedance spectra and can be modeled independently. The low-frequency contribution can be expressed as one resistive element R, accounting for the leakage of the material, and one capacitive C, accounting for the dielectric character. Conversely,

the high-frequency regime can be modeled in similar fashion, but the capacitive element is replaced by a constant phase element (CPE), which models the nonideal behavior of the capacitor. The impedance of this R CPE circuit is given by

$$Z^*_{R\text{-CPE}} = \frac{R}{[1 + RQ(iw)^{\alpha'}]}, \qquad (2)$$

where Q denotes the amplitude and α' deals with the phase of the CPE. The typical values range from $\alpha' \leq 0.6 - 1$, being $\alpha' = 1$ the value for an ideal capacitor, and in this case $C = Q$. Capacitance C and dielectric permittivity ε values can be obtained according to the relationship $C = (Q \times R)^{(1/\alpha')}/R$ [90], and $C = \varepsilon A/2t$, where A accounts for the area of the electrode and t for the thickness of the sample. It is important to remark, as mentioned before, that the nonideality of the capacitive response of the material can be qualitatively observed by the values of the α' variable in the CPE element. Therefore, the general behavior of the sample at any given temperature can be fitted by the
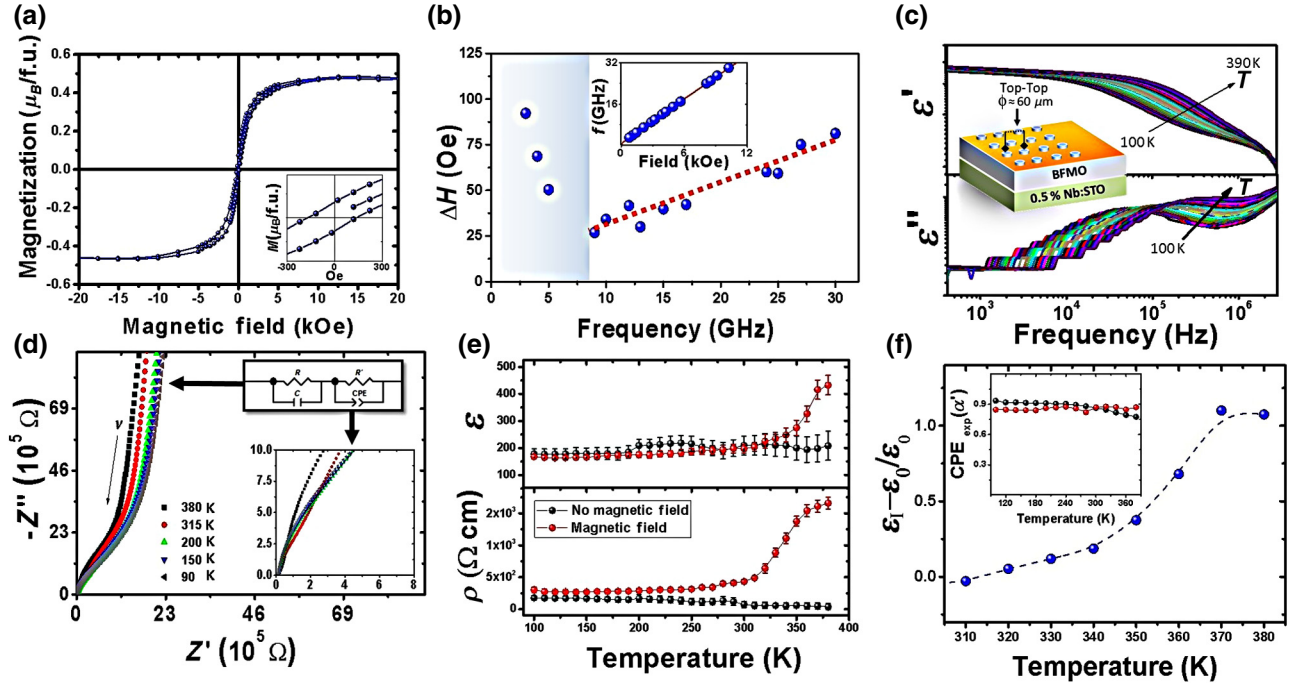
FIG. 3. Magnetic studies (a) SQUID magnetometry measurements $M(H)$ at 300 K. The inset shows the enlarged part of the hysteresis loop at low magnetic fields. (b) The FMR linewidth as a function of frequency. The shaded section marks the increase in FMR linewidth as a result of decreasing magnetization of the sample at corresponding fields. The inset shows the results of $f(H_r)$ dependence. Dielectric response of the BFMO thin films (c) overlapped dielectric spectra for ε' and ε'' for all the temperatures measured, the T arrow shows the trend as temperature increases. Inset shows a schematic of the measurement configuration. (d) Nyquist plots for selected spectra, showing the high- and low-frequency contributions. ν shows the frequency increment. Insets show the high-frequency regime and the associated circuit for each contribution. (e) Extracted values for the intrinsic dielectric permittivity (top) and resistivity (bottom) in the whole range of temperatures, for both magnetic and nonmagnetic measurements. (f) Dielectric permittivity (relative) changes as a function of temperature. Inset shows the values of the constant phase element (CPE) exponent(α') as a function of temperature with and without applied magnetic field.

following formula:

$$Z^* = \frac{R_I}{[1 + R_I Q_I (iw)^{\alpha'}]} + \frac{R_E}{(1 + R_E C_E iw)}, \qquad (3)$$

where the first term corresponds to the intrinsic (I) contribution of BFMO film and the second term deals with the extrinsic contributions (E). The two RC contributions of the equivalent circuit are sketched in the insets of Fig. 3(d), where the line through data points corresponds to the performed fitting showing the goodness of the fit, with values below $\chi^2 \leq 3 \times 10^{-4}$.

The extracted dielectric permittivity for each mechanism, allows the intrinsic contribution of the film to be further identified by its extracted value of the $\varepsilon = 175$, and resistivity $= 10^5$ Ω close to that previously reported in similar studies for the same compound [91]. The dielectric response remains constant in the whole range of temperature explored of 90–390 K.

However, when the spectroscopy measurements are repeated under external magnetic field (4 kOe) small changes on the spectroscopic response can be observed.

After extracting the associated dielectric value, a peak starting around 375 K can be observed [Fig. 3(e), top panel]. The dielectric permittivity peak under magnetic field [Fig. 3(f)] is accompanied by a large increase of resistance [Fig. 3(e), bottom panel]. This extraordinary increase of resistance under magnetic field can be ascribed to the semiconductor nature of the BFMO/Nb(0.5%) : SrTiO$_3$ junction that can result in large variations of resistance under magnetic field as reported elsewhere [92–94]. It is important to remark, that in both of the cases, with and without magnetic field, the exponent α' of the CPE element, remains relatively constant [see the inset of Fig. 3(f)], confirming the stable capacitive response of the film in the entire range examined.

D. Discussion

It is worthwhile to note the important differences and similarities between our samples and those previously reported in the literature. Sun *et al.* [51] have reported long-range B-site ordering on Bi$_2$FeMnO$_6$ films, however, the thickness of the films investigated is well above the relaxation point for the highly strained phase (190 nm).

Additionally, their magnetic studies showed unusually low magnetization, when compared with other works on highly strained BFMO thin films. The stoichiometry found in the aforementioned studies was the so-called vibronic ordering of Fe^{3+}-O-Mn^{3+} [80], which nominally would provide AFM to FM interactions, giving a total magnetization well below 0.02 μ_B/f.u.(Fe-Mn) at room temperature. The weak magnetism and strong ferroelectric response, suggest that the observed ordering is related to the previously observed bulk properties of BFMO [76]. Nevertheless, close inspection of previously reported, highly strained BFMO/STO films in the literature, shows the presence of similar features as the one described in this paper by HR TEM, but not addressed in their corresponding articles. Chen *et al.* [39] showed a complete study of the strain of BFMO films grown on several substrates and upon closer inspection, their SAED pattern, described in Ref. [39], shows faint, but clear peaks, similar to the ones reported in this article. Additionally, the same figure shows clear features as the ones shown here in Fig. 2(c) for the dark-field images. Li *et al.* [95], report on the interface effects of BFMO films, once again with a similar SAED pattern, shown in Ref. [95]. This seems to suggest that this feature is not in fact a casuistic or uncommon behavior of our film, but a generally overlooked feature in thin films of BFMO.

Regarding the origin of magnetic response in BFMO films, the Goodenough-Kanamori rules for 180° superexchange couplings can be evaluated. In principle, there are two possibilities for superexchange magnetism. First, the so-called vibronic FM to AFM ordering of Mn^{3+}-O-Mn^{3+} with a theoretical $\mu_{\mathrm{eff}} = 4\,\mu_B$/B-site ion for ferromagnetic ordering and the second one, so-called vibronic AFM to FM ordering of Fe^{3+}-O-Mn^{3+}, with a total magnetization of the 1 μ_B/B-site ion, none of which are in agreement with the data presented here or reported in the literature [34,39]. However, as shown previously in our XPS studies, the apparition of consistent Mn^{4+} across the sample, allows for the Mn^{4+}-O-Fe^{3+} FM to AFM [76]. Although it is still considerably higher than the theoretical 4.42 μ_B/f.u. for this ordered configuration, it is clear at this point that it is very complex to determine the true origin of the observed magnetization in BFMO. Nevertheless, recent studies have demonstrated the intrinsic role of the epitaxial strain on the origin of observed magnetization, suggesting the cooperative nature of both ferrimagnetic ordering and the Goodenough-Kanamori spin-canted effect at room temperature [34,39]. The role of oxygen vacancies in this matter is still unclear.

One of the most interesting aspect of this material, is relatively high magnetic transition temperature and its room-temperature ferroelectric response. Previous studies by Choi *et al.* [34], have shown a magnetic transition temperature around 600 K for the strained BFMO films. In our case, temperatures above 300 K are inaccessible, therefore, a rough estimation of the transition temperature is obtained

from the Weiss model, which provides a critical temperature T_C in the range 620 ± 80 K [Fig. S2 in Ref. [72]]. Nevertheless, the $M(H)$ plots confirm the ferromagnetic ordering of the film in the whole range of available temperatures, as shown by the hysteresis loops at room temperature, Fig. 3(a) and 10 K [Fig. S2 in Ref. [72]]. On the other hand, the dielectric studies clearly show an anomaly that seems not to follow the estimated magnetic transition temperature of the strained films (620 ± 80 K). Impedance spectroscopy measurements, tend to show erratic behavior when close to the magnetic transition giving unclear results about magnetodielectric coupling effects. However, in this case, such phenomena can be ruled out, due to no evident variation of the dielectric permittivity with the absence of external magnetic field. Nonetheless, the clear correlation between the applied external magnetic field and the anomalous dielectric response at high-temperature points to a strong magnetodielectric coupling [87] well above room temperature Fig. 3(f), which, in addition to the room-temperature ferroelectric [54] and ferromagnetic character of BFMO, makes BFMO interesting for applications.

IV. CONCLUSION

In conclusion, we investigate the dielectric and magnetic properties of highly strained $Bi(Fe_{0.5}Mn_{0.5})O_3$ (001)/$SrTiO_3$(001) thin films. Films show strong room-temperature magnetic response, attributed to the ferromagnetic ordering and spin-canting effect of the STO(001) interface. Magnetic transition temperature is estimated to be around 620 ± 80 K with a room-temperature magnetic saturation of 68.8 emu/cm³ (0.44 μ_B/f.u.). Furthermore, our dielectric studies show an anomalous response of the dielectric permittivity under external magnetic field that clearly suggest above room-temperature magnetodielectric coupling. Additionally to the room-temperature magnetization, the low Gilbert damping ($\alpha = 0.0034$) observed in BFMO, not only places them among the low Gilbert damping materials, but also positions it as one of a kind (ferroelectric and ferromagnetic) multiferroic perovskite with low damping. These facts offer a new perspective in the field of spin-transfer-torque devices as the Gilbert constant appears to be lower than in commonly employed permalloy [96] or (Co, Fe)B [55,97] films. Moreover, large relaxation times combined with magnetodielectric coupling can potentially be used for voltage-driven excitation and control of spin waves [57,98,99]. The phenomena observed is attributed to strain induced on the epitaxial growth and its quantum-mechanical origin should be further investigated.

[1] Nicola A. Spaldin, Multiferroics: Past, present, and future, MRS Bull. **42**, 385 (2017).

[2] Junjiro Kanamori, Superexchange interaction and symmetry properties of electron orbitals, J. Phys. Chem. Solids **10**, 87 (1959).

[3] Tôru Moriya, Anisotropic superexchange interaction and weak ferromagnetism, Phys. Rev. **120**, 91 (1960).

[4] Masaki Azuma, Kazuhide Takata, Takashi Saito, Shintaro Ishiwata, Yuichi Shimakawa, and Mikio Takano, Designed ferromagnetic, ferroelectric Bi_2NiMnO_6, J. Am. Chem. Soc. **127**, 8889 (2005).

[5] Daniel I. Khomskii, Multiferroics: Different ways to combine magnetism and ferroelectricity, J. Magn. Magn. Mater. **306**, 1 (2006).

[6] Z. H. Chi, H. Yang, S. M. Feng, F. Y. Li, R. C. Yu, and C. Q. Jin, Room-temperature ferroelectric polarization in multiferroic $BiMnO_3$, J. Magn. Magn. Mater. **310**, e358 (2007).

[7] Silvia Picozzi, Kunihiko Yamauchi, Ivan A. Sergienko, Cengiz Sen, Biplab Sanyal, and Elbio Dagotto, Microscopic mechanisms for improper ferroelectricity in multiferroic perovskites: A theoretical review, J. Phys. Condens. Matter **20**, 434208 (2008).

[8] H. Guo, J. Burgess, E. Ada, S. Street, A. Gupta, M. Iliev, A. Kellock, C. Magen, M. Varela, and S. Pennycook, Influence of defects on structural and magnetic properties of multifunctional La_2NiMnO_6 thin films, Phys. Rev. B **77**, 174423 (2008).

[9] M. Hashisaka, D. Kan, A. Masuno, M. Takano, Y. Shimakawa, T. Terashima, and K. Mibu, Epitaxial growth of ferromagnetic La_2NiMnO_6 with ordered double-perovskite structure, Appl. Phys. Lett. **89**, 032504 (2006).

[10] S. Kazan, F. A. Mikailzade, M. Özdemir, B. Aktaş, B. Rameev, A. Intepe, and A. Gupta, Ferromagnetic resonance in double perovskite epitaxial thin films of La_2NiMnO_6 on $SrTiO_3$ and $NdGaO_3$ substrates, Appl. Phys. Lett. **97**, 072511 (2010).

[11] M. Kitamura, I. Ohkubo, M. Kubota, Y. Matsumoto, H. Koinuma, and M. Oshima, Ferromagnetic properties of epitaxial La_2NiMnO_6 thin films grown by pulsed laser deposition, Appl. Phys. Lett. **94**, 132506 (2009).

[12] Y. Q. Lin, X. M. Chen, and X. Q. Liu, Relaxor-like dielectric behavior in La_2NiMnO_6 double perovskite ceramics, Solid. State. Commun. **149**, 784 (2009).

[13] N. S. Rogado, J. Li, A. W. Sleight, and M. A. Subramanian, Magnetocapacitance and magnetoresistance near room temperature in a ferromagnetic semiconductor: La_2NiMnO_6, Adv. Mater. **17**, 2225 (2005).

[14] M. Singh, K. Truong, S. Jandl, and P. Fournier, Long-range Ni/Mn structural order in epitaxial double perovskite La_2NiMnO_6 thin films, Phys. Rev. B **79**, 224421 (2009).

[15] K. Truong, M. Singh, S. Jandl, and P. Fournier, Influence of Ni/Mn cation order on the spin-phonon coupling in multifunctional La_2NiMnO_6 epitaxial films by polarized Raman spectroscopy, Phys. Rev. B **80**, 134424 (2009).

[16] L. E. Coy, I. Fina, J. Ventura, L. Yate, E. Langenberg, M. C. Polo, C. Ferrater, and M. Varela, Dielectric characterization of multiferroic magnetoelectric double-perovskiteY $(Ni_{0.5}Mn_{0.5})O_3$ thin films, Appl. Phys. Lett. **109**, 152901 (2016).

[17] Sanjeev Kumar, Gianluca Giovannetti, Jeroen van den Brink, and Silvia Picozzi, Theoretical prediction of multiferroicity in double perovskite Y_2NiMnO_6, Phys. Rev. B **82**, 134429 (2010).

[18] Raimundo Bezerra Macedo Filho, Alejandro Pedro Ayala, and Carlos William de Araujo Paschoal, Spin-phonon coupling in Y_2NiMnO_6 double perovskite probed by Raman spectroscopy, Appl. Phys. Lett. **102**, 192902 (2013).

[19] R. P. Maiti, S. Dutta, M. Mukherjee, M. K. Mitra, and Dipankar Chakravorty, Magnetic and dielectric properties of sol-gel derived nanoparticles of double perovskite Y_2NiMnO_6, J. Appl. Phys. **112**, 044311 (2012).

[20] G. Sharma, T. S. Tripathi, J. Saha, and S. Patnaik, Magnetic entropy change and critical exponents in double perovskite Y_2NiMnO_6, J. Magn. Magn. Mater. **368**, 318 (2014).

[21] M. H. Tang, Y. G. Xiao, B. Jiang, J. W. Hou, J. C. Li, and J. He, The giant dielectric tunability effect in bulk Y_2NiMnO_6 around room temperature, Appl. Phys. A **105**, 679 (2011).

[22] Changzheng Xie and Lei Shi, Tuning of magnetic properties for epitaxial Y_2NiMnO_6 thin film: Substrate is crucial, Appl. Surf. Sci. **384**, 459 (2016).

[23] Adrian Ciucivara, Bhagawan Sahu, and Leonard Kleinman, Density functional study of multiferroic Bi_2NiMnO_6, Phys. Rev. B **76**, 064412 (2007).

[24] M. Iliev, P. Padhan, and A. Gupta, Temperature-dependent Raman study of multiferroic Bi_2NiMnO_6 thin films, Phys. Rev. B **77**, 172303 (2008).

[25] E. Langenberg, M. Varela, M. V. García-Cuenca, C. Ferrater, M. C. Polo, I. Fina, L. Fàbrega, F. Sánchez, and J. Fontcuberta, Epitaxial thin films of $(Bi_{0.9}La_{0.1})_2NiMnO_6$ obtained by pulsed laser deposition, J. Magn. Magn. Mater. **321**, 1748 (2009).

[26] E. Langenberg, J. Rebled, S. Estradé, C. J. M. Daumont, J. Ventura, L. E. Coy, M. C. Polo, M. V. García-Cuenca, C. Ferrater, B. Noheda, F. Peiró, M. Varela, and J. Fontcuberta, Long-range order of Ni^{2+} and Mn^{4+} and ferromagnetism in multiferroic $(Bi_{0.9}La_{0.1})_2NiMnO_6$ thin films, J. Appl. Phys. **108**, 123907 (2010).

[27] P. Padhan, P. LeClair, A. Gupta, and G. Srinivasan, Magnetodielectric response in epitaxial thin films of multiferroic Bi_2NiMnO_6, J. Phys. Condens. Matter **20,** 355003 (2008).

[28] N. E. Rajeevan, Ravi Kumar, D. K. Shukla, P. Thakur, N. B. Brookes, K. H. Chae, W. K. Choi, S. Gautam, S. K. Arora, I. V. Shvets, and P. P. Pradyumnan, Bi-substitution-induced magnetic moment distribution in spinel $BiCo_2MnO_4$ multiferroic, J. Phys. Condens. Matter **21,** 406006 (2009).

[29] Abduleziz Ablat, Emin Muhemmed, Cheng Si, Jiaou Wang, Haijie Qian, Rui Wu, Nian Zhang, Rong Wu, and Kurash Ibrahim, Electronic structure of $BiFe_{1−x}Mn_xO_3$ thin films investigated by x-ray absorption spectroscopy, J. Nanomater. **2012,** 1 (2012).

[30] Towfiq Ahmed, Aiping Chen, Dmitry A. Yarotski, Stuart A. Trugman, Quanxi Jia, and Jian-Xin Zhu, Magnetic, electronic, and optical properties of double perovskite Bi_2FeMnO_6, APL Mater. **5,** 035601 (2017).

[31] Alexei A. Belik, Artem M. Abakumov, Alexander A. Tsirlin, Joke Hadermann, Jungeun Kim, Gustaaf Van Tendeloo, and Eiji Takayama-Muromachi, Structure and magnetic properties of $BiFe_{0.75}Mn_{0.25}O_3$ perovskite prepared at ambient and high pressure, Chem. Mater. **23,** 4505 (2011).

[32] Lei Bi, Alexander Taussig, Hyun-Suk Kim, Lei Wang, Gerald Dionne, D. Bono, K. Persson, Gerbrand Ceder, and C. Ross, Structural, magnetic, and optical properties of $BiFeO_3$ and Bi_2FeMnO_6 epitaxial thin films: An experimental and first-principles study, Phys. Rev. B **78,** 104106 (2008).

[33] C. A. Bridges, A. S. Sefat, E. A. Payzant, L. Cranswick, and M. P. Paranthaman, Structure and magnetic order in the series $Bi_xRE_{1−x}Fe_0.5Mn_0.5O_3$ (RE=La, Nd), J. Solid. State. Chem. **184,** 830 (2011).

[34] E.-M. Choi, S. Patnaik, E. Weal, S.-L. Sahonta, H. Wang, Z. Bi, J. Xiong, M. G. Blamire, Q. X. Jia, and J. L. MacManus-Driscoll, Strong room temperature magnetism in highly resistive strained thin films of $BiFe_{0.5}Mn_{0.5}O_3$, Appl. Phys. Lett. **98,** 012509 (2011).

[35] D. L. Cortie, A. P. J. Stampfl, F. Klose, Y. Du, X. L. Wang, H. Y. Zhao, H. Kimura, and Z. X. Cheng, The magnetic structure of an epitaxial $BiMn_{0.5}Fe_{0.5}O_3$ thin film on $SrTiO_3$ (001) studied with neutron diffraction, Appl. Phys. Lett. **101,** 172404 (2012).

[36] S. Malo, C. Lepoittevin, O. Pérez, S. Hébert, G. Van Tendeloo, and M. Hervieu, Incommensurate crystallographic shear structures and magnetic properties of the cation deficient perovskite $(Sr_{0.61}Pb_{0.18})(Fe_{0.75}Mn_{0.25})O_{2.29}$, Chem. Mater. **22,** 1788 (2010).

[37] V. G. Prokhorov, G. G. Kaminsky, J. M. Kim, Y. J. Yoo, Y. P. Lee, V. L. Svetchnikov, G. G. Levchenko, Yu. M. Nikolaenko, and V. A. Khokhlov, Evidence of the Griffiths phase in multiferroic $BiMnO_3$ and $BiFe_{0.5}Mn_{0.5}O_3$ films, Low Temp. Phys. **38,** 413 (2012).

[38] Gustau Catalan and James F. Scott, Physics and applications of bismuth ferrite, Adv. Mater. **21,** 2463 (2009).

[39] Wei-Fu Chen, James T. Muckerman, and Etsuko Fujita, Recent developments in transition metal carbides and nitrides as hydrogen evolution electrocatalysts, Chem. Commun. **49,** 8896 (2013).

[40] M. Gajek, M. Bibes, A. Barthélémy, K. Bouzehouane, S. Fusil, M. Varela, J. Fontcuberta, and A. Fert, Spin filtering through ferromagnetic $BiMnO_3$ tunnel barriers, Phys. Rev. B **72,** 020406 (2005).

[41] T. Kimura, S. Kawamoto, I. Yamada, M. Azuma, M. Takano, and Y. Tokura, Magnetocapacitance effect in multiferroic $BiMnO_3$, Phys. Rev. B **67,** 180401 (2003).

[42] Alexei A. Belik, Origin of magnetization reversal and exchange bias phenomena in solid solutions of $BiFeO_3$-$BiMnO_3$: Intrinsic or extrinsic? Inorg. Chem. **52,** 2015 (2013).

[43] Claude Ederer and Craig J. Fennie, Electric-fields witchable magnetization via the Dzyaloshinskii-Moriya interaction: $FeTiO_3$ versus $BiFeO_3$, J. Phys. Condens. Matter **20,** 434219 (2008).

[44] Jinwon Jeong, Han-Jin Noh, and Sung Baek Kim, Effects of structural distortion induced by Sc substitution in $LuFe_2O_4$, J. Korean Phys. Soc. **64,** 1701 (2014).

[45] Junghwan Park, Sang-Hyun Lee, Seongsu Lee, Fabia Gozzo, Hiroyuki Kimura, Yukio Noda, Young Jai Choi, Valery Kiryukhin, Sang-Wook Cheong, Younjung Jo, Eun Sang Choi, Luis Balicas, Gun Sang Jeon, and Je-Geun Park, Magnetoelectric feedback among magnetic order, polarization, and lattice in multiferroic $BiFeO_3$, J. Phys. Soc. Jpn. **80,** 114714 (2011).

[46] Ivan A. Sergienko, Cengiz Şen, and Elbio Dagotto, Ferroelectricity in the Magnetic *E*-Phase of Orthorhombic Perovskites, Phys. Rev. Lett. **97,** 227204 (2006).

[47] M. Grizalez, E. Martinez, J. Caicedo, J. Heiras, and P. Prieto, Occurrence of ferroelectricity in epitaxial $BiMnO_3$ thin films, Microelectronics J. **39,** 1308 (2008).

[48] Z. H. Chi, C. J. Xiao, S. M. Feng, F. Y. Li, C. Q. Jin, X. H. Wang, R. Z. Chen, and L. T. Li, Manifestation of ferroelectromagnetism in multiferroic $BiMnO_3$, J. Appl. Phys. **98,** 103519 (2005).

[49] E. Langenberg, I. Fina, J. Ventura, B. Noheda, M. Varela, and J. Fontcuberta, Dielectric properties of $(Bi_{0.9}La_{0.1})_2NiMnO_6$ thin films: Determining the intrinsic electric and magnetoelectric response, Phys. Rev. B **86,** 085108 (2012).

[50] Bing-Cheng Luo, Chang-Le Chen, Zhi Xu, and Qian Xie, Effect of Cr substitution on the multiferroic properties of $BiFe_{1−x}Cr_xO_3$ compounds, Phys. Lett. A **374,** 4265 (2010).

[51] Lin Sun, Yue-Wen Fang, Jun He, Yuanyuan Zhang, Ruijuan Qi, Qing He, Rong Huang, Pinghua Xiang, Xiao-Dong Tang, Pingxiong Yang, Junhao Chu, Ying-Hao Chu, and Chun-Gang Duan, The preparation, and structural and multiferroic properties of B-site ordered double-perovskite Bi_2FeMnO_6, J. Mater. Chem. C **5,** 5494 (2017).

[52] Rainer Schmidt, Jofre Ventura, Eric Langenberg, Norbert M. Nemes, Carmen Munuera, Manuel Varela, Mar Garcia-Hernandez, Carlos Leon, and Jacobo Santamaria, Magnetoimpedance spectroscopy of epitaxial multiferroic thin films, Phys. Rev. B **86,** 035113 (2012).

[53] Adelina Ianculescu, Felicia Prihor Gheorghiu, Petronel Postolache, Ovidiu Oprea, and Liliana Mitoseriu, The role of doping on the structural and functional properties of $BiFe_{1−x}Mn_xO_3$ magnetoelectric ceramics, J. Alloys Compd. **504,** 420 (2010).

[54] Eun-Mi Choi, Thomas Fix, Ahmed Kursumovic, Christy J. Kinane, Darío Arena, Suman-Lata Sahonta, Zhenxing Bi, Jie Xiong, Li Yan, Jun-Sik Lee, Haiyan Wang, Sean Langridge, Young-Min Kim, Albina Y. Borisevich, Ian

MacLaren, Quentin M. Ramasse, Mark G. Blamire, Quanxi Jia, and Judith L. MacManus-Driscoll, Room temperature ferrimagnetism and ferroelectricity in strained, thin films of $BiFe_{0.5}Mn_{0.5}O_3$, Adv. Funct. Mater. **24**, 7478 (2014).

[55] A. Conca, T. Nakano, T. Meyer, Y. Ando, and B. Hillebrands, CoFeAlB alloy with low damping and low magnetization as a candidate for spin transfer torque switching, J. Appl. Phys. **122**, 073902 (2017).

[56] Jack C. Sankey, Yong-Tao Cui, Jonathan Z. Sun, John C. Slonczewski, Robert A. Buhrman, and Daniel C. Ralph, Measurement of the spin-transfer-torque vector in magnetic tunnel junctions, Nat. Phys. **4**, 67 (2008).

[57] P. Rovillain, R. de Sousa, Y. Gallais, A. Sacuto, M. A. Méasson, D. Colson, A. Forget, M. Bibes, A. Barthélémy, and M. Cazayous, Electric-field control of spin waves at room temperature in multiferroic $BiFeO_3$, Nat. Mater. **9**, 975 (2010).

[58] D. Sando, A. Agbelele, D. Rahmedov, J. Liu, P. Rovillain, C. Toulouse, I. C. Infante, A. P. Pyatakov, S. Fusil, E. Jacquet, C. Carrétéro, C. Deranlot, S. Lisenkov, D. Wang, J.-M. Le Breton, M. Cazayous, A. Sacuto, J. Juraszek, A. K. Zvezdin, L. Bellaiche, B. Dkhil, A. Barthélémy, and M. Bibes, Crafting the magnonic and spintronic response of $BiFeO_3$ films by epitaxial strain, Nat. Mater. **12**, 641 (2013).

[59] E. Langenberg, M. Varela, M. V. García-Cuenca, C. Ferrater, F. Sánchez, and J. Fontcuberta, Thin films in ternary Bi-Mn-O system obtained by pulsed laser deposition, Mater. Sci. Eng. B **144**, 138 (2007).

[60] H. Gowiński, M. Schmidt, I. Gościańska, J.-Ph. Ansermet, and J. Dubowik, Coplanar waveguide based ferromagnetic resonance in ultrathin film magnetic nanostructures: Impact of conducting layers, J. Appl. Phys. **116**, 053901 (2014).

[61] I. Fina, L. Fàbrega, E. Langenberg, X. Martií, F. Sànchez, M. Varela, and J. Fontcuberta, Nonferroelectric contributions to the hysteresis cycles in manganite thin films: A comparative study of measurement techniques, J. Appl. Phys. **109**, 074105 (2011).

[62] Bo Wha Lee, Pil Sun Yoo, Vu Binh Nam, Kirstie Raquel Natalia Toreh, and Chang Uk Jung, Magnetic and electric properties of stoichiometric $BiMnO_3$ thin films, Nanoscale Res. Lett. **10**, 47 (2015).

[63] R. Jarrier, X. Marti, J. Herrero-Albillos, P. Ferrer, R. Haumont, P. Gemeiner, G. Geneste, P. Berthet, T. Schülli, P. Cevc, R. Blinc, Stanislaus S. Wong, Tae-Jin Park, M. Alexe, M. A. Carpenter, J. F. Scott, G. Catalan, and B. Dkhil, Surface phase transitions in $BiFeO_3$ below room temperature, Phys. Rev. B **85**, 184104 (2012).

[64] C. M. Raghavan, J. W. Kim, H. J. Kim, W. J. Kim, and S. S. Kim, Preparation and properties of rare earth (Eu, Tb, Ho) and transition metal (Co) co-doped $BiFeO_3$ thin films, J. Solgel. Sci. Technol. **64**, 178 (2012).

[65] Yogesh Sharma, Radhe Agarwal, Charudatta Phatak, Bumsoo Kim, Seokwoo Jeon, Ram S. Katiyar, and Seungbum Hong, Long-range stripe nanodomains in epitaxial(110) $BiFeO_3$ thin films on (100) $NdGaO_3$ substrate, Sci. Rep. **7**, 4857 (2017).

[66] J. Wang, Epitaxial $BiFeO_3$ multiferroic thin film heterostructures, Science **299**, 1719 (2003).

[67] M. W. Lufaso and P. M. Woodward, Prediction of the crystal structures of perovskites using the software program *SPuDS*, Acta Crystallogr. B Struct. Sci. **57**, 725 (2001).

[68] Andrey A. Voevodin, Jeffrey S. Zabinski, John G. Jones, and David P. Norton, *Pulsed Laser Deposition of Thin Films: Applications-Led Growth of Functional Materials, edited by Robert Eason* (John Wiley & Sons, Inc., Hoboken, NJ, USA, 2006), p. 585.

[69] Javier Fernández Sanjulián, Madhu Chennabasappa, Susana García-Martín, Gwilherm Nénert, Alain Wattiaux, Etienne Gaudin, and Olivier Toulemonde, Oxygen vacancy ordering in $SrFe_{0.25}Co_{0.75}O_{2.63}$ perovskite material, Dalton Trans. **46**, 1624 (2017).

[70] Guiju Liu, Xiaotian Li, Yiqian Wang, Wenshuang Liang, Bin Liu, Honglei Feng, Huaiwen Yang, Jing Zhang, and Jirong Sun, Nanoscale domains of ordered oxygen-vacancies in $LaCoO_3$ films, Appl. Surf. Sci. **425**, 121 (2017).

[71] Sheng Xu, Yong Qin, Chen Xu, Yaguang Wei, Rusen Yang, and Zhong Lin Wang, Self-powered nanowire devices, Nat. Nanotechnol. **5**, 366 (2010).

[72] See Supplemental Material at http://link.aps.org/supplemental/10.1103/PhysRevApplied.10.054072 for XPS spectra, magnetic measurements, FMR spectra, and comparison of damping constants.

[73] Thomas P. Debies and J. Wayne Rabalais, X-ray photoelectron spectra and electronic structure of Bi_2X_3 (X = O, S, Se, Te), Chem. Phys. **20**, 277 (1977).

[74] Mark C. Biesinger, Brad P. Payne, Andrew P. Grosvenor, Leo W. M. Lau, Andrea R. Gerson, and Roger St. C. Smart, Resolving surface chemical states in XPS analysis of first row transition metals, oxides and hydroxides: Cr, Mn, Fe, Co and Ni, Appl. Surf. Sci. **257**, 2717 (2011).

[75] Toru Yamashita and Peter Hayes, Analysis of XPS spectra of Fe^{2+} and Fe^{3+} ions in oxide materials, Appl. Surf. Sci. **254**, 2441 (2008).

[76] Towfiq Ahmed, Aiping Chen, Brian McFarland, Qiang Wang, Hendrik Ohldag, Richard Sandberg, Quanxi Jia, Dmitry A. Yarotski, and Jian-Xin Zhu, Site-mixing effect on the XMCD spectrum in double perovskite Bi_2FeMnO_6, Appl. Phys. Lett. **108**, 242907 (2016).

[77] Ming-Wen Chu, Marcel Ganne, Maria Teresa Caldes, and Luc Brohan, X-ray photoelectron spectroscopy and high resolution electron microscopy studies of Aurivillius compounds: $Bi_{4-x}La_xTi_3O_{12}$ ($x = 0$, 0.5, 0.75, 1.0, 1.5, and 2.0), J. Appl. Phys. **91**, 3178 (2002).

[78] F. Song, Å Monsen, Z. S. Li, E.-M. Choi, J. L. MacManus-Driscoll, J. Xiong, Q. X. Jia, E. Wahlström, and J. W. Wells, Extracting the near surface stoichiometry of $BiFe_{0.5}Mn_{0.5}O_3$ thin films; A finite element maximum entropy approach, Surf. Sci. **606**, 1771 (2012).

[79] I. MacLaren, B. Sala, S. M. L. Andersson, T. J. Pennycook, J. Xiong, Q. X. Jia, E.-M. Choi, and J. L. MacManus-Driscoll, Strain localization in thin films of Bi(Fe, Mn)O_3 due to the formation of stepped Mn^{4+}-rich antiphase boundaries, Nanoscale Res. Lett. **10**, 407 (2015).

[80] P. Mandal, Shridevi S. Bhat, Y. Sundarayya, A. Sundaresan, C. N. R. Rao, V. Caignaert, B. Raveau, and E. Suard, Structure and complex magnetic behavior of disordered perovskite $(Bi_{0.5}Sr_{0.5})(Fe_{0.5}Mn_{0.5})O_3$, RSC Adv. **2**, 292 (2012).

[81] Aidan J. Lee, Jack T. Brangham, Yang Cheng, Shane P. White, William T. Ruane, Bryan D. Esser, David W. McComb, P. Chris Hammel, and Fengyuan Yang, Metallic ferromagnetic films with magnetic damping under 1.4×10^{-3}, Nat. Commun. **8**, 1 (2017).

[82] B. Manjunath, P. Thakuria, and P. A. Joy, Structural, magnetic, dielectric and magnetodielectric properties of $Bi_{1-x}Ca_xFe_{1-x}Mn_xO_3$ in the morphotropic phase boundary region, Mater. Res. Express **4**, 016104 (2017).

[83] L. M. Garten, P. Lam, D. Harris, J.-P. Maria, and S. Trolier-McKinstry, Residual ferroelectricity in barium strontium titanate thin film tunable dielectrics, J. Appl. Phys. **116**, 044104 (2014).

[84] Ashok Kumar, N. M. Murari, and R. S. Katiyar, Diffused phase transition and relaxor behavior in $Pb(Fe_{2/3}W_{1/3})O_3$ thin films, Appl. Phys. Lett. **90**, 162903 (2007).

[85] Y. P. Shi and A. K. Soh, Modeling of enhanced electrocaloric effect above the Curie temperature in relaxor ferroelectrics, Acta. Mater. **59**, 5574 (2011).

[86] Muhammad Usman, Arif Mumtaz, Sobia Raoof, and S. K. Hasanain, Magnetic control of relaxor features in $BaZr_{0.5}Ti_{0.5}O_3$ and $CoFe_2O_4$ composite, Appl. Phys. Lett. **102**, 112911 (2013).

[87] G. Catalan, Magnetocapacitance without magnetoelectric coupling, Appl. Phys. Lett. **88**, 102902 (2006).

[88] Rainer Schmidt, Wilma Eerenstein, Thomas Winiecki, Finlay Morrison, and Paul Midgley, Impedance spectroscopy of epitaxial multiferroic thin films, Phys. Rev. B **75**, 245111 (2007).

[89] L. E. Coy, I. Fina, J. Ventura, L. Yate, E. Langenberg, M. C. Polo, C. Ferrater, and M. Varela, Dielectric characterization of multiferroic magnetoelectric double-perovskite $Y(Ni_{0.5}Mn_{0.5})O_3$ thin films, Appl. Phys. Lett. **109**, 152901 (2016).

[90] Frank Berkemeier, Mohammad Abouzari, and Guido Schmitz, Thickness-dependent dc conductivity of lithium borate glasses, Phys. Rev. B **76**, 024205 (2007).

[91] J. Miao, X. Zhang, Q. Zhan, Y. Jiang, and K.-H. Chew, Bi-relaxation behaviors in epitaxial multiferroic double-perovskite $BiFe_{0.5}Mn_{0.5}O_3/CaRuO_3$ heterostructures, Appl. Phys. Lett. **99**, 062905 (2011).

[92] Zhaochu Luo, Chengyue Xiong, Xu Zhang, Zhen-Gang Guo, Jianwang Cai, and Xiaozhong Zhang, Extremely large magnetoresistance at low magnetic field by coupling the nonlinear transport effect and the anomalous Hall effect, Adv. Mater. **28**, 2760 (2016).

[93] Dezheng Yang, Fangcong Wang, Yang Ren, Yalu Zuo, Yong Peng, Shiming Zhou, and Desheng Xue, A large magnetoresistance effect in p–n junction devices by the space-charge effect, Adv. Funct. Mater. **23**, 2918 (2013).

[94] Jiaojiao Chen, Xiaozhong Zhang, Zhaochu Luo, Jimin Wang, and Hong-Guang Piao, Large positive magnetoresistance in germanium, J. Appl. Phys. **116**, 114511 (2014).

[95] Leigang Li, Wenrui Zhang, Fauzia Khatkhatay, Jie Jian, Meng Fan, Qing Su, Yuanyuan Zhu, Aiping Chen, Ping Lu, Xinghang Zhang, and Haiyan Wang, Strain and interface effects in a novel bismuth-based self-assembled supercell structure, ACS. Appl. Mater. Interfaces. **7**, 11631 (2015).

[96] Yuelei Zhao, Qi Song, See-Hun Yang, Tang Su, Wei Yuan, Stuart S. P. Parkin, Jing Shi, and Wei Han, Experimental investigation of temperature-dependent Gilbert damping in permalloy thin films, Sci. Rep. **6**, 22890 (2016).

[97] Piotr Kuświk, Hubert Gowiński, Emerson Coy, Janusz Dubowik, and Feliks Stobiecki, Perpendicularly magnetized $Co_{20}Fe_{60}B_{20}$ layer sandwiched between Au with low Gilbert damping, J. Phys. Condens. Matter **29**, 435803 (2017).

[98] Sergiy Cherepov, Pedram Khalili Amiri, Juan G. Alzate, Kin Wong, Mark Lewis, Pramey Upadhyaya, Jayshankar Nath, Mingqiang Bao, Alexandre Bur, Tao Wu, Gregory P. Carman, Alexander Khitun, and Kang L. Wang, Electric-field-induced spin wave generation using multiferroic magnetoelectric cells, Appl. Phys. Lett. **104**, 082403 (2014).

[99] A. V. Sadovnikov, A. A. Grachev, E. N. Beginin, S. E. Sheshukova, Yu. P. Sharaevskii, and S. A. Nikitov, Voltage-controlled spin-wave coupling in adjacent ferromagnetic-ferroelectric heterostructures, Phys. Rev. Appl. **7**, 014013 (2017).